Aerodynamic Investigation of Fan-in-Wing Propulsion at Low Reynolds Numbers for Micro Aerial Vehicles

Burhan Saeed* and Matthew Chong Ping†
Aerospace Engineering, University of Nottingham, United Kingdom

ABSTRACT

The Solar Swifter SS1 is a promising conceptual micro aerial vehicle (MAV) at $Re = 5 \times 10^4$ combining fixed-wing endurance with fan-in-wing (FIW) VTOL capability. No quantitative aerodynamic basis for FIW design at this Reynolds number currently exists. This paper presents a parametric CFD study on a low aspect ratio NACA 0009 wing with two embedded fans, using the γ-Re_θ transition model, validated within 5% over $0^\circ \leq \alpha \leq 6^\circ$ with qualitative wind tunnel support. Fan diameter, spanwise position, chordwise position, and thrust were varied to produce a screening-level C_L/C_D dataset. The 35 mm inboard rear-chord configuration achieved best lift to drag ratio of 11.60 at 20 g of thrust per fan. At 1–3 g of thrust per fan, a net power saving was predicted at $\alpha = 5^\circ$ above a certain fan efficiency, suggesting FIW potential as an active flow control mechanism beyond VTOL. The results inform future SS1 aerofoil co-design for low-Reynolds-number FIW integration.

1 INTRODUCTION

Micro aerial vehicles (MAVs) are commonly characterised as aircraft with a maximum mass of 0.1 kg and a characteristic dimension no greater than 0.15 m [1]. Their compact size enables deployment in surveillance, environmental monitoring, and search-and-rescue operations within confined or hazardous environments inaccessible to larger platforms [2]. Among the three principal MAV configurations, fixed-wing designs offer the greatest endurance for a given mass — the Black Widow achieves 30 minutes of flight at 80 g [3], compared to only 10 minutes at 90 g for the rotary-wing QRW100S [2] — owing to the ability of a fixed wing to generate lift passively through forward motion. Rotary-wing platforms, conversely, provide hover and vertical take-off and landing (VTOL) capability, broadening operational utility in environments where precise station-keeping is essential, while flapping-wing designs offer bio-inspired manoeuvrability but remain mechanically complex with limited payload capacity [4].

No single configuration therefore satisfies the full range of operational demands placed on modern MAVs, motivating hybrid concepts that combine the cruise endurance of fixed-wing flight with the VTOL and hover capability of rotary systems. The Solar Swifter SS1, conceived by Saeed [1], is one such concept: a solar-powered MAV featuring ultra-thin photovoltaic panels mounted on a low aspect ratio wing ($1 \leq AR \leq 2$), with a predicted mass of 51 g, cruise speed of 9 ms^{-1}, and chordwise Reynolds number of $Re = 5 \times 10^4$, placing it within the transitional flow regime. The key specifications of the SS1 are summarised in Table 1.

1.1 The Solar Swifter SS1: Concept and Design Rationale

With only 1.9 W of available solar power, the SS1 is severely power-constrained, making the maximisation of cruise endurance the primary aerodynamic design objective. VTOL capability is achieved through three ducted fan-in-wing units embedded within the wing planform: two symmetric wing-mounted fans provide vertical thrust and lateral stability, while a rear fan governs thrust and pitch control. Forward propulsion is provided by a nose-mounted propeller, and the overall configuration is illustrated in Figure 1.

Table 1: Solar Swifter SS1 design specifications.

Parameter	Value
Total mass	51 g
Aspect ratio	$1 \leq AR \leq 2$
Cruise speed	9 ms^{-1}
Reynolds number	$Re = 5 \times 10^4$
Available solar power	1.9 W
Propulsion (VTOL)	3× ducted fan-in-wing fans
Propulsion (cruise)	Nose-mounted propeller
Wing geometry	Low aspect ratio with PV panels
Flow regime	Transitional

Fan-in-wing propulsion embeds ducted fans within the wing structure, ingesting flow from the upper surface and ejecting a high-momentum jet below, altering the surrounding flow field relative to the fan-off case. Understanding how fan geometry influences lift augmentation and cruise efficiency is therefore a prerequisite for improving the endurance and operational range of the SS1. Existing FIW studies are predominantly conducted at $Re \geq 10^6$ [5, 6], where laminar separation bubbles — characteristic of MAV-scale aerodynamics — are largely absent. At the Reynolds numbers relevant to MAV operation ($Re \leq 1 \times 10^5$), there remains a significant gap in quantitative data describing the influence of fan diameter, chordwise position, spanwise position, and thrust coefficient

*Email address: Burhan.Saeed@nottingham.ac.uk
†Email address: egymc7@nottingham.ac.uk

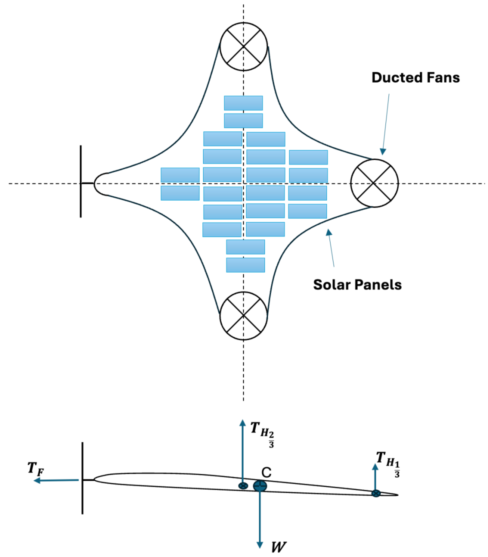

Figure 1: A schematic layout of Solar Swifter SS1 concept (taken from [1]) .

on lift, drag, and stall behaviour [1].

The interaction between the embedded fan jet, the transitional boundary layer, and the low-aspect-ratio wingtip vortex has not been systematically characterised, and to the authors' knowledge no published quantitative aerodynamic basis exists for FIW design at MAV-scale Reynolds numbers. This paper addresses that gap with the following aim: to establish screening-level aerodynamic trends describing how fan geometry affects lift augmentation and cruise efficiency of a FIW configuration at $Re = 5 \times 10^4$, and to assess whether FIW operation can yield a net power benefit at the SS1 cruise condition.

To achieve this, an $AR = 2$ NACA 0009 finite wing with two embedded fans is adopted as a controlled aerodynamic model, chosen in preference to the full SS1 planform — which was under concurrent development — to isolate the aerodynamic effects of fan geometry. A parametric CFD study varying fan diameter, chordwise position, spanwise position, and thrust coefficient produces a quantitative dataset of C_L, C_D, and C_L/C_D trends. The numerical methodology is validated against wind tunnel testing to confirm that the CFD captures the principal aerodynamic trends. Finally, a first-order cruise power analysis is applied to evaluate whether FIW operation produces a net system power benefit under SS1 cruise conditions.

2 Low Reynolds Number and Low Aspect Ratio Challenges

At $Re = 5 \times 10^4$, the laminar boundary layer separates under an adverse pressure gradient and can reattach as a turbulent shear layer, forming a laminar separation bubble (LSB) [7, 8, 9]. The LSB introduces a chordwise pressure plateau, reducing lift and increasing drag through poorer pressure recovery [8, 10]. Winslow et al. report bubble extents of 15–40% chord in the range $10^4 < Re < 10^5$, with trailing-edge bursting producing abrupt stall [10], while Giacomini and Westerberg show that purely turbulent RANS closures fail to capture LSB onset correctly [11]. Since fan operation modifies the local pressure field, a transition-sensitive model is required to ensure fan-induced aerodynamic changes are not misattributed to modelling error.

For the SS1, $AR = 2$ is adopted as a controlled baseline within the identified optimal range $1 \leq AR \leq 2$. The classical induced drag relation,

$$C_{D,i} = \frac{C_L^2}{\pi e AR} \tag{1}$$

where e is the Oswald efficiency factor, illustrates the inverse dependence of induced drag on aspect ratio. Torres and Mueller demonstrate that aspect ratio is the dominant performance parameter in this regime, with Reynolds number as a secondary influence [12]. At low aspect ratios, strong wingtip vortices distort the spanwise lift distribution and produce inherently three-dimensional flow, yielding softer stall characteristics than equivalent two-dimensional aerofoils [7]. Spanwise fan position may therefore alter the interaction between the embedded jet, the local downwash, and the wingtip vortex, with consequent effects on lift augmentation and induced drag.

3 Numerical Modeling at Low Reynolds Number

Direct numerical simulation (DNS) and large eddy simulation (LES) are excluded on grounds of computational cost given the number of parametric operating points. Instead, the steady Reynolds-averaged Navier-Stokes (RANS) equations are solved with the γ-Re_θ transition model of Langtry and Menter [13]. Purely turbulent closures are unsuitable at $Re = 5 \times 10^4$ because large regions of the wing remain laminar; such models trigger transition prematurely and fail to capture LSB onset correctly. The γ-Re_θ model addresses this through coupled transport equations for intermittency γ and the transition-onset Reynolds number $\widetilde{Re}_{\theta t}$, suppressing eddy viscosity in laminar regions and permitting transition to turbulent flow where the local flow conditions demand it.

Both Liu et al. [14] and Giacomini and Westerberg [11] assessed transition models at $Re \leq 1 \times 10^5$, finding that the γ-Re_θ model outperforms the k-k_L-ω and k-ω SST closures in capturing LSB onset and stall behaviour; Giacomini and Westerberg further demonstrated that it correctly predicts stall onset where purely turbulent models fail entirely [11]. Regarding inlet conditions, prior validation studies report accurate results from turbulence intensities as low as $Tu = 0.3\%$ [15]. As the wind tunnel turbulence intensity is not precisely characterised, $Tu = 0.5\%$ is adopted as a conservative estimate. The γ-Re_θ model at $Tu = 0.5\%$ is therefore employed throughout the parametric CFD study as a practical transition-sensitive RANS closure.

4 Methodology

4.1 Computational Setup

The reference geometry was a NACA 0009 aerofoil with chord $c = 76.2$ mm and span $b = 152.4$ mm, giving $AR = 2$. A freestream velocity of $V_\infty = 9.6$ ms^{-1} was applied throughout all studies, corresponding to $Re = 5 \times 10^4$ and matching the SS1 cruise condition.

The steady RANS equations were solved with the γ-Re_θ transition model of Langtry and Menter [13], using a pseudo-transient coupled pressure–velocity scheme with second-order upwind discretisation. Inlet conditions were set to $Tu = 0.5\%$, $\gamma = 0$, and $\mu_t/\mu = 1$, prescribing a laminar incoming boundary layer consistent with low-turbulence external flow. Convergence was declared when scaled residuals fell below 1×10^{-4} and C_L, C_D, and fan inlet mass flow rate had stabilised.

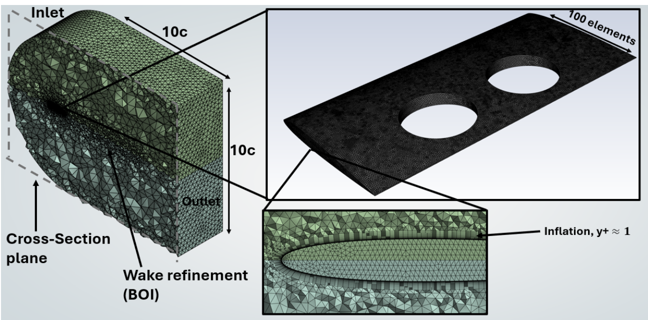

Figure 2: Computational mesh for the $AR = 2$ NACA 0009 finite wing showing the C-type domain, wake refinement, and near-wall inflation layer ($y^+ \approx 1$).

A C-type structured mesh with a near-wall inflation layer sized to $y^+ \approx 1$ was applied, with 100 chordwise elements and body-of-influence wake refinement (Figure 2). Independence studies confirmed differences below 2.7% in C_L and 1.7% in C_D relative to the finest mesh, with domain sensitivity below 0.15% (Tables 2–3). These deviations are smaller than the parametric trends of interest; absolute coefficients are treated as indicative.

The embedded fans were modelled via a uniform static pressure-jump boundary condition with swirl from propeller momentum theory, capturing the macro-scale fan–wing aerodynamic interaction without resolving duct-internal flow. Force coefficients were integrated over all wing surfaces including duct walls, representing the fan-induced aerodynamic effect rather than total propulsive force. The thrust vector is excluded from the aerodynamic comparison and incorporated separately in the cruise power analysis.

Table 2: Mesh independence study results for the $AR = 2$ NACA 0009 finite wing at $Re = 5 \times 10^4$.

Parameter	Coarse	Medium	Fine
Elements ($\times 10^6$)	1.8	4.0	8.0
C_L	0.232	0.229	0.226
C_D	0.03100	0.03080	0.03070
ΔC_L vs. fine (%)	−2.71	−1.26	—
ΔC_D vs. fine (%)	−1.73	−0.64	—

Table 3: Domain independence study results for the $AR = 2$ NACA 0009 finite wing at $Re = 5 \times 10^4$.

Parameter	Small	Medium	Large
Domain vol. (c^3)	56.25	200	4220
Elements ($\times 10^6$)	2.8	3.0	5.5
C_L	0.3507	0.3405	0.3409
C_D	0.04713	0.04656	0.04660
ΔC_L vs. large (%)	−2.89	+0.11	—
ΔC_D vs. large (%)	−1.13	+0.10	—

4.2 Wind Tunnel Setup

The numerical methodology was validated experimentally using the TecQuipment AF100 wind tunnel at $V_\infty \approx 9.5$ ms^{-1}, corresponding to $Re \approx 5 \times 10^4$. The wind tunnel model featured a NACA 0024 section with chord $c = 76.2$ mm and span $b = 152.4$ mm; the thicker profile was selected to accommodate the fan motor geometry within the wing without surface protrusion. The model was 3D-printed and subsequently sanded to minimise surface roughness effects. Two 35 mm brushless fans were installed at the mid-chord, inboard spanwise position and powered via an electronic speed controller (ESC) from a lithium polymer (LiPo) battery, as shown in Figure 3.

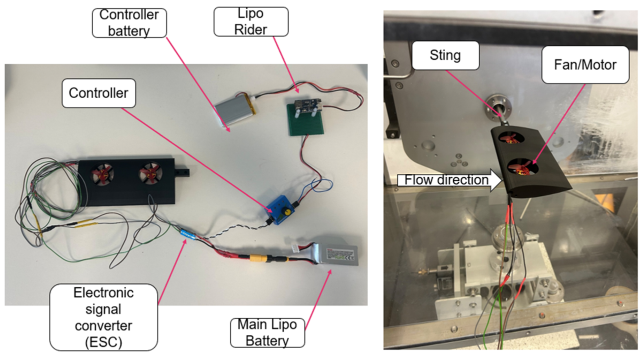

Figure 3: Wind tunnel model: (*a*) NACA 0024 3D-printed wing with 35 mm embedded fans and electronics, and (*b*) sting-mounted model installed on the TecQuipment AF100 force balance.

Fan thrust was set by static tare on the force balance with the tunnel off. The model was mounted on a sting connected to the force balance, and the angle of attack was varied from 0° to 40° in increments of 5° to 10°. At each angle, force data were recorded at 2 Hz for 120 s and time-averaged to reduce random error. A matched NACA 0024 CFD case was run to ensure the experimental comparison used an identical aerofoil geometry.

Force measurement uncertainty was estimated by combining the tunnel-off tare instability, $u_{\text{tare}} = 0.0140$ N, with the standard deviation of the force signal during each 120 s wind-on run, u_{run}, as:

$$u_F = \sqrt{u_{\text{tare}}^2 + u_{\text{run}}^2} \tag{2}$$

yielding typical values of $u_{F,L} \approx 0.015$ N and $u_{F,D} \approx 0.015$ N, shown as error bars on the lift comparison plots. Systematic contributions from sting interference, wiring drag, and angle-dependent weight projection could not be independently quantified.

Drag measurements are excluded from the validation. The measured drag exceeds the CFD prediction by $+0.188$ N at $\alpha = 0°$ and exhibits a non-physical trend, decreasing from $\alpha = 0°$ to $20°$ before rising, which is inconsistent with expected low-Reynolds-number behaviour. The experimental validation is therefore based on lift alone, assessing the pre-stall lift slope, peak lift location, and post-stall trend against the matched CFD case.

5 RESULTS AND ANALYSIS

5.1 *Validation*

The γ-Re_θ model was validated in 2D against the experimental C_L–α data of Lutz and Würz [15] for a NACA 0009 aerofoil at $Re = 5 \times 10^4$ (Figure 4). Agreement was within 5% over $0° \leq \alpha \leq 6°$ with accurate stall angle prediction at $\alpha = 9°$, though C_L was underpredicted by approximately 15% near stall, consistent with the known behaviour of steady RANS in separated flow [11]. This agreement was considered acceptable for a screening-level study.

The 3D methodology was assessed against wind tunnel measurements on the NACA 0024 model at $Re \approx 5 \times 10^4$ and a nominal static thrust of 30 g (Figure 5). Both CFD and experiment show C_L increasing monotonically to a peak near $\alpha = 35°$ followed by a post-stall reduction. A crossover is observed: the experiment exceeds CFD by 0.06–0.07 N at low incidence, while CFD overpredicts by approximately 0.08 N near $\alpha = 35°$. Discrepancies are attributed to the simplified pressure-jump fan model, sting interference, surface roughness, and wiring drag. The CFD nonetheless reproduces the pre-stall lift slope, peak lift location, and post-stall trend with sufficient fidelity, providing qualitative support for the γ-Re_θ framework at this Reynolds number. Quantitative validation on a matched NACA 0009 geometry remains a priority for future work.

Figure 6 shows the flow field for the baseline FIW configuration prior to the parametric study, illustrating the high-momentum jet beneath the wing and the wingtip vortices characteristic of low-aspect-ratio operation at $Re = 5 \times 10^4$. These features provide physical context for the force coefficient trends discussed in the following sections.

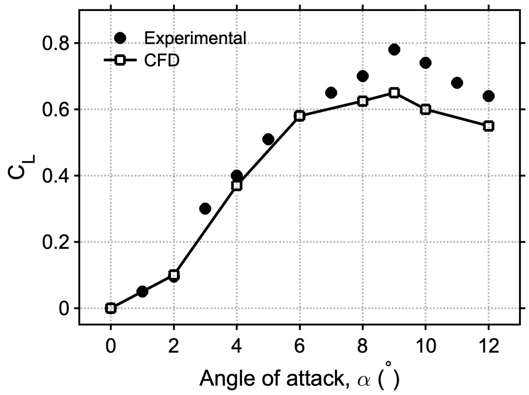

Figure 4: C_L versus α for a NACA 0009 aerofoil at $Re = 5 \times 10^4$: CFD predictions against experimental data of Lutz and Würz [15].

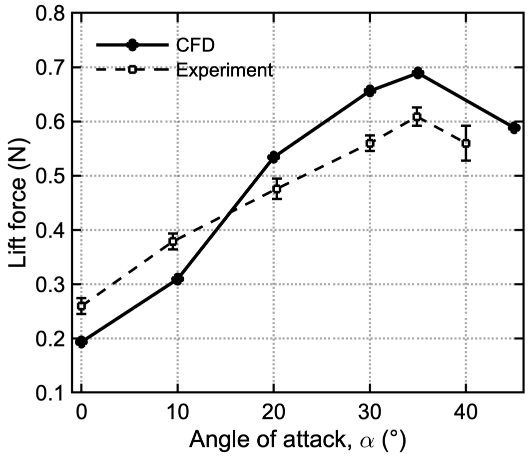

Figure 5: Lift force versus α for the NACA 0024 finite wing at $Re \approx 5 \times 10^4$ with a nominal static thrust of 30 g: CFD predictions against wind tunnel measurements. Error bars denote combined force uncertainty u_F; thrust vector excluded from lift integration.

5.2 *Inlet Diameter*

The 35 mm and 45 mm configurations produced comparable C_L/C_D across the full angle of attack range, while the 25 mm fan was consistently the weakest in the cruise regime despite generating the highest C_L at high incidence (Figure 7). At $\alpha = 10°$, the 25 mm configuration achieved $C_L/C_D = 5.86$, approximately 18% below the 35 mm value of 7.12. Above $\alpha = 20°$, all three configurations converged.

The weaker cruise performance of the 25 mm fan is consistent with its higher jet velocity at equal thrust. From actuator disk theory, the 25 mm fan produces a jet velocity of 31.1 ms^{-1}, compared with 22.4 ms^{-1} for the 35 mm and 17.4 ms^{-1} for the 45 mm fan. Velocity contours confirm that the 25 mm jet penetrates more deeply into the freestream (Figure 8), consistent with greater jet–freestream interaction

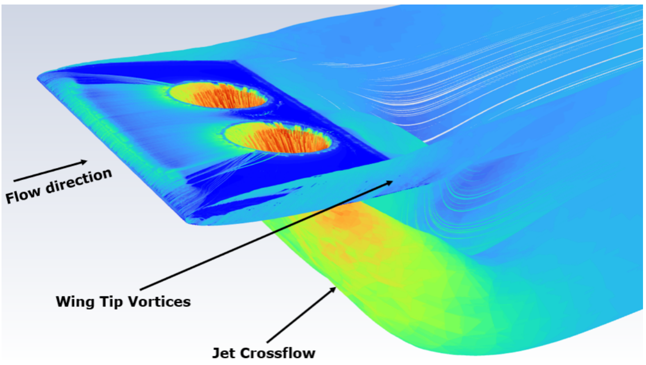

Figure 6: Velocity contours for the baseline FIW configuration at $\alpha = 5°$ and $Re = 5 \times 10^4$, showing the fan exhaust jet beneath the wing and wingtip vortices.

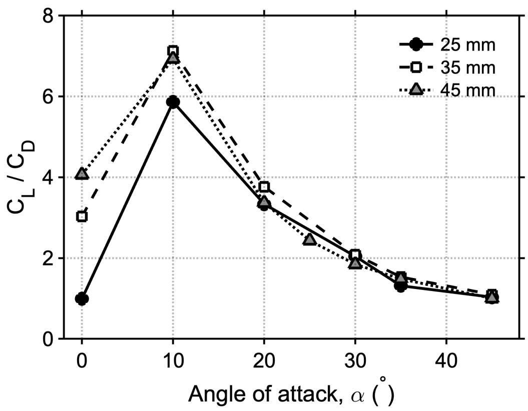

Figure 7: C_L/C_D versus α for fan inlet diameters of 25, 35, and 45 mm at the mid-span, mid-chord position; 30 g per fan, $Re = 5 \times 10^4$, thrust vector excluded from force integration.

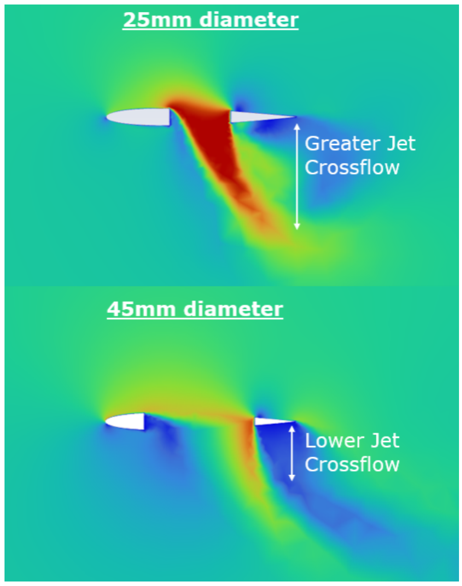

Figure 8: Velocity magnitude contours at $\alpha = 0°$ for 25 mm and 45 mm fan inlet diameters, showing increased jet–freestream interaction at the smaller diameter; 30 g per fan, $Re = 5 \times 10^4$, mid-span mid-chord position.

and an increased drag penalty relative to the circulation benefit. Since the 35 mm and 45 mm configurations produced similar C_L/C_D — with differences approaching mesh sensitivity bounds — the 35 mm diameter was selected for subsequent studies on the basis of easier structural integration within the NACA 0009 profile.

5.3 Spanwise Position

The inboard fan position produced the highest C_L/C_D across the operational range (Figure 9). At $\alpha = 0°$, the inboard configuration achieved $C_L/C_D = 5.24$, compared with 3.03 for mid-span and 2.53 for outboard, with the inboard advantage maintained throughout the cruise regime. Between the inboard and outboard cases at $\alpha = 0°$, C_L decreased by 29% and C_D increased by 46%. Above $\alpha = 20°$, all configurations converged. At $\alpha = 20°$, the outboard configuration produced the highest C_L, reversing the low-incidence ranking; the physical basis for this reversal is not fully resolved within the present dataset.

The superior inboard performance is consistent with wingtip-vortex-induced downwash reducing the effective local angle of attack at outboard stations. Vorticity contours on a transverse plane at the trailing edge show the fan exit vortex structures merging with the wingtip vorticity field in the outboard configuration, while the inboard configuration maintains distinct separated structures (Figure 10), consistent with greater tip-vortex influence at the outboard fan inlet station; quantitative confirmation would require further wake analysis. The inboard position was selected for subsequent studies, though concentrating fan operation inboard may have adverse implications for the SS1 lateral stability requirements.

5.4 Chordwise Position

Chordwise placement introduced a design trade-off rather than a single optimum (Figure 11). At $\alpha = 0°$, rear placement achieved $C_L/C_D = 6.90$ against 4.75 for mid-chord. At $\alpha = 10°$, this ranking reversed: mid-chord achieved $C_L/C_D = 8.36$ against 7.10 for the rear case, while rear placement produced higher lift at $C_L = 1.427$ compared with 0.878 for mid-chord, a 62% increase. Neither configuration therefore dominates across the full cruise regime: rear placement is superior at low incidence ($\alpha = 0°$ to 5°), while mid-chord produces higher C_L/C_D at $\alpha = 10°$. Above $\alpha = 20°$, both configurations converged as stall-associated pressure drag became governing.

The lift advantage of rear placement is consistent with a jet-flap-like circulation augmentation effect, though direct comparison with the $Re \sim 10^6$ results of Thouault et al. [5] is limited by the different boundary-layer regime at $Re = 5 \times 10^4$, where laminar separation dynamics may modify the

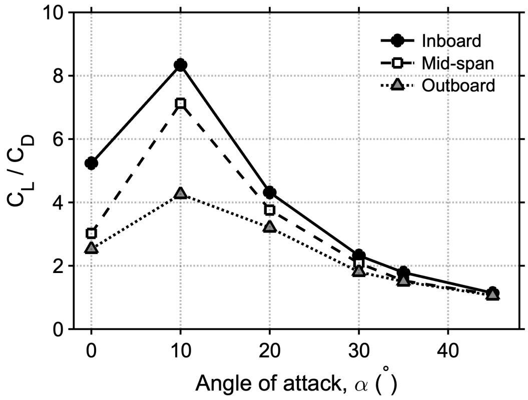

Figure 9: C_L/C_D versus α for fan inlet diameters of 25, 35, and 45 mm at the mid-span, mid-chord position; 30 g per fan, $Re = 5 \times 10^4$, thrust vector excluded from force integration.

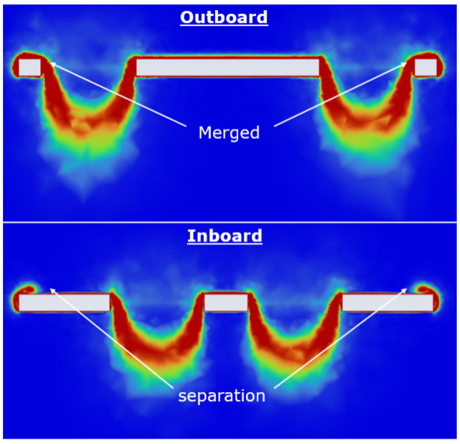

Figure 10: Vorticity magnitude on a transverse plane at the fan inlet station for inboard and outboard spanwise positions at $\alpha = 10°$; 35 mm fans, 30 g per fan, $Re = 5 \times 10^4$, mid-chord position.

aerodynamic response; surface pressure measurements would be required to confirm the mechanism. The forward placement ($x/c = 1/3$) could not be assessed as stable convergence was not achievable within the pseudo-transient framework, possibly due to unsteady leading-edge separation. The rear configuration was selected for the thrust sweep as it produced superior C_L/C_D at the low-incidence cruise condition most representative of the SS1 ($\alpha = 0°$ to $5°$).

5.5 *Thrust Sweep*

Fan thrust was varied from fan-off to 30 g per fan on the 35 mm inboard rear-chord configuration in discrete increments, with finer resolution at low thrust levels. The aerodynamic coefficients reported throughout exclude the direct thrust vector, isolating the fan-induced aerodynamic effect on the wing surfaces. Fan-on operation produces a clear aerodynamic benefit relative to the fan-off baseline across the cruise

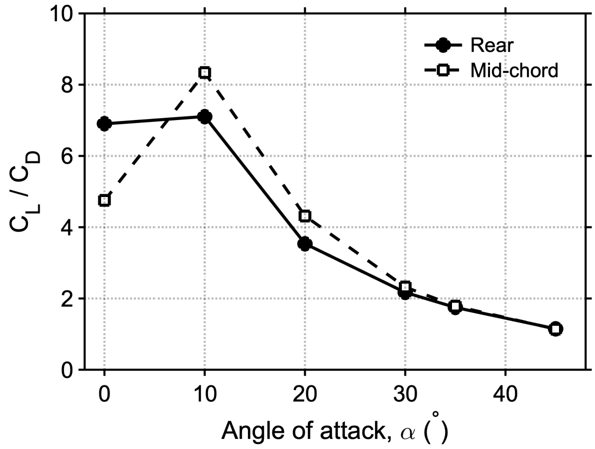

Figure 11: C_L/C_D versus α for mid-chord and rear-chord fan positions; 35 mm inboard fans, 30 g per fan, $Re = 5 \times 10^4$, thrust vector excluded from force integration.

regime (Figure 12). At $\alpha = 0°$, the fan-off symmetric section generates no lift; at just 5 g per fan, C_L/C_D reaches 4.40, demonstrating that even modest thrust produces meaningful aerodynamic benefit through fan-induced modification of the wing flow field. At $\alpha = 10°$, C_L/C_D increases from 5.26 at fan-off to 6.34 at 5 g — a 20% improvement — with further gains to 7.11 at 15 g.

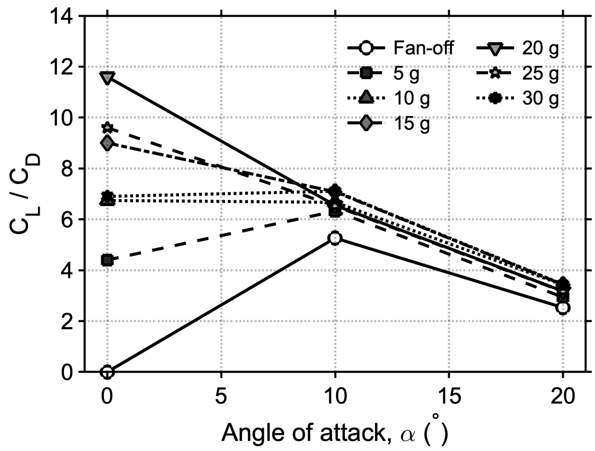

Figure 12: C_L/C_D versus α for fan thrust levels of 0–30 g per fan; 35 mm inboard rear-chord configuration, $Re = 5 \times 10^4$, thrust vector excluded from force integration.

Aerodynamic efficiency does not increase indefinitely with thrust. At $\alpha = 0°$, C_L/C_D rises to a peak of 11.60 at 20 g per fan, beyond which efficiency declines to 9.60 at 25 g and 7.11 at 30 g (Figure 13), indicating that beyond 20 g additional thrust introduces drag disproportionately relative to the lift gain. At moderate incidence ($\alpha = 10°$), C_L/C_D remains broadly invariant with thrust, ranging between 6.17 and 7.11 across the full sweep, indicating that additional thrust increases lift and drag in similar proportion. By $\alpha = 20°$, C_L/C_D converges to 2.5–3.5 across all thrust levels as stall-dominated pressure drag becomes governing.

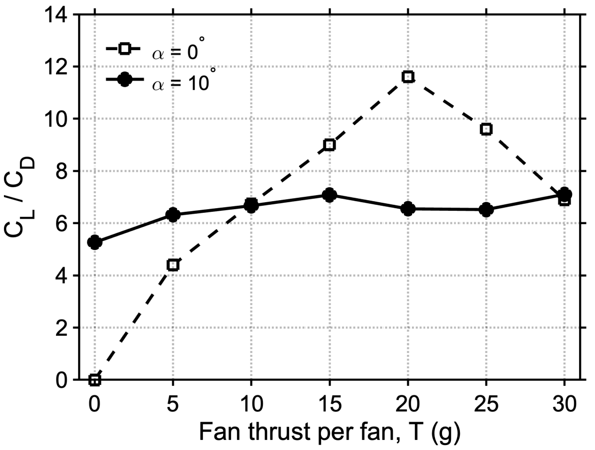

Figure 13: C_L/C_D versus fan thrust per fan at $\alpha = 0°$ and $\alpha = 10°$; 35 mm inboard rear-chord configuration, $Re = 5 \times 10^4$, thrust vector excluded from force integration.

5.6 *Cruise Power Analysis*

An iso-lift power comparison was performed for thrust levels of 1–5 g per fan at $\alpha = 0°$ and $\alpha = 5°$, with results presented at a fan-system efficiency of $\eta = 0.4$ as a representative engineering estimate for small-scale fans. At $\alpha = 5°$, fan-on configurations from 1 to 5 g per fan produce lower total system power than the fan-off baseline at equivalent lift across the valid comparison range (Figure 14). The fan-off baseline rises steeply as it approaches its stall lift limit of 0.395 N, indicated by the dashed vertical line.

At $\alpha = 5°$ and $\eta = 0.40$, total system power for the fan-on cases is approximately 190, 342, and 430 mW at 1, 2, and 3 g per fan respectively, compared with fan-off equivalent powers of approximately 334, 548, and 863 mW, giving net savings of approximately 144, 206, and 433 mW under the assumed actuator-disk model. It should be noted that at higher thrust levels the fan-on total lift approaches the fan-off stall limit, making the apparent saving increasingly favourable by virtue of a poor fan-off reference rather than genuine fan-on benefit. These values should not be interpreted as predicted savings for the finalised SS1 design, as the final planform will most likely employ a cambered aerofoil at lower cruise incidence, which would reduce or eliminate the apparent benefit.

All five thrust cases cross zero below $\eta = 0.15$, confirming that a net power saving is achievable provided the installed fan-system efficiency meets this threshold (Figure 15). The 1–3 g range is the most credible operating regime, as the comparison is made against a fan-off baseline well within the pre-stall regime where the saving is genuine rather than a consequence of an unfavourable fan-off reference point. Whether installed fan-system efficiency meets the breakeven threshold

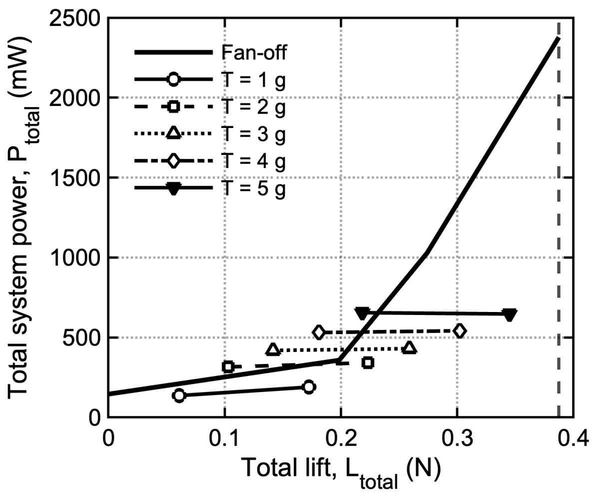

Figure 14: Total system power versus total lift for fan thrust levels of 1–5 g per fan and the fan-off baseline at $\alpha = 5°$; $\eta = 0.40$, thrust vector included in force integration. Dashed line indicates the fan-off stall lift limit (0.395 N).

at off-design thrust settings cannot be confirmed without motor characterisation data.

6 CONCLUSIONS

A parametric CFD study at $Re = 5 \times 10^4$ has addressed a gap in quantitative aerodynamic guidance for low-Reynolds-number FIW MAV design. The principal findings are:

- The γ-Re_θ model achieved 2D validation within 5% over $0° \leq \alpha \leq 6°$ with accurate stall prediction; wind tunnel testing provided qualitative support for the 3D FIW methodology, with discrepancies attributed to the simplified fan boundary condition.
- Spanwise position had the largest geometric influence: the inboard configuration outperformed the outboard by approximately 40% in C_L/C_D at $\alpha = 0°$, consistent with tip-vortex downwash suppressing jet-induced circulation at the outboard inlet.
- Rear-chord placement produced trends consistent with jet-flap circulation augmentation, outperforming mid-chord at low incidence. The 35 mm inlet outperformed the 25 mm at equal thrust, consistent with lower jet velocity and reduced jet–freestream interaction.
- The 35 mm inboard rear-chord configuration achieved peak efficiency of $C_L/C_D = 11.60$ at 20 g per fan ($\alpha = 0°$, thrust vector excluded); beyond 20 g, drag growth exceeded the lift benefit.
- At 1–3 g per fan, a net system power saving was predicted at $\alpha = 5°$ provided $\eta \geq 0.15$, suggesting FIW potential as an active flow control mechanism beyond VTOL.

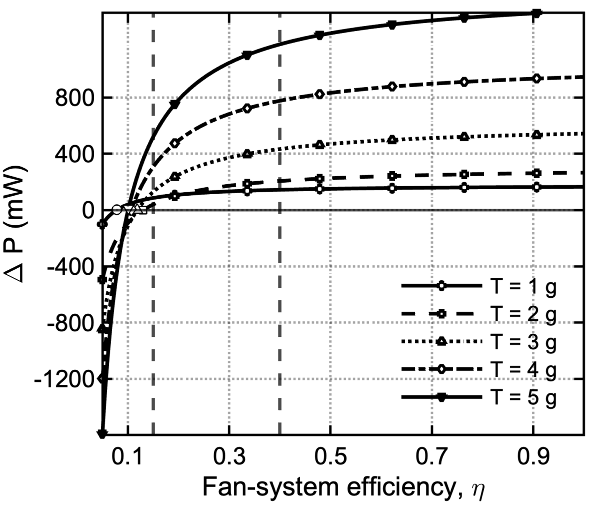

Figure 15: Net power saving ΔP versus fan-system efficiency η at $\alpha = 5°$ for fan thrust levels of 1–5 g per fan; open markers denote the breakeven efficiency $\eta_{\min}$.

These results are based on a simplified symmetric planform and should not be extrapolated directly to the finalised SS1 design; a cambered aerofoil at lower cruise incidence may reduce or eliminate the predicted power saving.

REFERENCES

[1] B. Saeed and P. Thomas. Feasibility study of a solar powered hybrid micro-aerial vehicle. In *15th International Micro Air Vehicle Conference and Competition (IMAV 2024)*, 2024.

[2] L. Petricca, P. Ohlckers, and C. Grinde. Micro- and nano-air vehicles: State of the art. *International Journal of Aerospace Engineering*, 2011:1–17, 2011.

[3] J.M. Grasmeyer and M.T. Keennon. Development of the black widow micro air vehicle. In *39th AIAA Aerospace Sciences Meeting and Exhibit*, 2001.

[4] N. Haider, A. Shahzad, M.N. Mumtaz Qadri, and S.I. Ali Shah. Recent progress in flapping wings for micro aerial vehicle applications. *Proceedings of the Institution of Mechanical Engineers, Part C: Journal of Mechanical Engineering Science*, 235(2):245–264, 2021.

[5] N. Thouault, C. Gologan, C. Breitsamter, and N.A. Adams. Aerodynamic investigations on a generic fan-in-wing configuration. In *26th International Congress of the Aeronautical Sciences (ICAS 2008)*, Anchorage, AK, USA, 2008.

[6] N. Thouault, C. Breitsamter, N.A. Adams, C. Gologan, and J. Seifert. Experimental investigation of the aerodynamic characteristics of generic fan-in-wing configurations. *Aeronautical Journal*, 113(1139):9–20, 2009.

[7] G.K. Ananda, P.P. Sukumar, and M.S. Selig. Measured aerodynamic characteristics of wings at low reynolds numbers. *Aerospace Science and Technology*, 42:392–406, 2015.

[8] J. Wauters and J. Degroote. On the study of transitional low-reynolds number flows over airfoils operating at high angles of attack and their prediction using transitional turbulence models. *Progress in Aerospace Sciences*, 103:52–68, 2018.

[9] T.J. Mueller and J.D. DeLaurier. Aerodynamics of small vehicles. *Annual Review of Fluid Mechanics*, 35(1):89–111, 2003.

[10] J. Winslow, H. Otsuka, B. Govindarajan, and I. Chopra. Basic understanding of airfoil characteristics at low reynolds numbers (10^4–10^5). *Journal of Aircraft*, 55(3):1050–1061, 2018.

[11] E. Giacomini and L.-G. Westerberg. Cfd analysis of transition models for low-reynolds number aerodynamics. *Applied Sciences*, 15(18):10299, 2025.

[12] G.E. Torres and T.J. Mueller. Low aspect ratio aerodynamics at low reynolds numbers. *AIAA Journal*, 42(5):865–873, 2004.

[13] R.B. Langtry and F.R. Menter. Correlation-based transition modeling for unstructured parallelized γ-re_θ computational fluid dynamics codes. *AIAA Journal*, 47(12):2894–2906, 2009.

[14] Y. Liu, P. Li, and K. Jiang. Comparative assessment of transitional turbulence models for airfoil aerodynamics in the low reynolds number range. *Journal of Wind Engineering and Industrial Aerodynamics*, 217:104726, 2021.

[15] Th. Lutz and W. Wurz. Numerical optimization and wind tunnel testing of low reynolds number airfoils. In *Low Reynolds Number Aerodynamics and Transition*, Stuttgart, Germany. University of Stuttgart.